Journal Pre-proofs

Insights into the optoelectronic and thermoelectric properties of lead-free Rb$_2$NaIF$_6$ double perovskite compound: A first-principles study

Mwende Mbilo, Robinson Musembi, John Peter Kachira, Winfrey Nyongesa Onsata, Fanuel Mugwanga Kubasu, Refilwe Edwin Mapasha

PII: S2211-3797(25)00240-8
DOI: https://doi.org/10.1016/j.rinp.2025.108349
Reference: RINP 108349

To appear in: *Results in Physics*

Received Date: 3 May 2025
Revised Date: 26 June 2025
Accepted Date: 1 July 2025

Please cite this article as: Mbilo, M., Musembi, R., Kachira, J.P., Onsata, W.N., Kubasu, F.M., Mapasha, R.E., Insights into the optoelectronic and thermoelectric properties of lead-free Rb$_2$NaIF$_6$ double perovskite compound: A first-principles study, *Results in Physics* (2025), doi: https://doi.org/10.1016/j.rinp.2025.108349

Insights into the Optoelectronic and Thermoelectric Properties of Lead-Free Rb_2NaInF_6 Double Perovskite Compound: A First-Principles Study

Masinde Mbiti[a,*], Robinson Musembi[b], John Peter Kachiro[a,c], Wesley Nyangau Onsate[a], Fanuel Mugwanga Keheze[a], Refilwe Edwin Mapasha[d]

[a]Department of Physics and Sustainable Technology, School of Pure and Applied Sciences, Pwani University, P.O. Box 195-80108, Kilifi, Kenya

[b]Materials Research Group, Department of Physics, Faculty of Science and Technology, University of Nairobi, P.O. Box 30197 – 00100, Nairobi, Kenya

[c]Department of Physics, Mbeya University of Science and Technology, P.O. Box 131, Mbeya, Tanzania

[d]Department of Physics, University of Pretoria, Hatfield campus, Pretoria 0002, South Africa

*Corresponding Author: [illegible]

Abstract

This study investigated the structural, electronic, elastic, mechanical, thermodynamic, optical, and thermoelectric properties of the Rb_2NaInF_6 lead-free double perovskite compound using first-principles methods. The structural stability of the perovskite was confirmed by the Goldschmidt tolerance and octahedral factors. Dynamic stability was confirmed through the negative energy of formation and positive frequency modes of the phonon dispersion curve. The dynamic stability results suggest that the studied compound could be potentially synthesized experimentally. The Rb_2NaInF_6 compound is a direct semiconductor with electronic band gaps within the range of 2.14-3.78 eV, computed using different approximations. The mechanical stability was confirmed by the elastic calculation results. The Rb_2NaInF_6 compound was found to be ductile, ionic, and anisotropic. The optical properties showed that Rb_2NaInF_6 strongly absorbs light in the ultraviolet region, which is desirable for ultraviolet-photosensitive materials in optoelectronic devices. The computed thermoelectric figure of merit of the Rb_2NaInF_6 compound is 0.81 at 1000 K, suggesting high thermoelectric efficiency. These findings demonstrate the potential of Rb_2NaInF_6 lead-free double perovskite compound for optoelectronic and thermoelectric applications. Therefore, our investigation offers theoretical insights that can lead to the experimental synthesis and study of Rb_2NaInF_6 lead-free double perovskites.

Keywords: DFT, GGA, double perovskites, optoelectronics, thermoelectric applications

1. Introduction

Researchers have been striving to develop efficient and cost-effective materials for harvesting solar radiation and converting it to electrical energy. Perovskites are among the most extensively investigated materials for optoelectronic and thermoelectric applications. These compounds are well known for their excellent properties, including tunable electronic band gaps, structural stability, and high absorption coefficients [1]. Their versatile properties have enabled their applications in various fields, including solar cells, photocatalysis, refrigeration, reflective coatings, water splitting, smart windows, spintronics, and thermoelectric power devices [2–10]. Lead halide perovskite solar cells have shown remarkable progress in recent years, reaching efficiencies exceeding 25% [11]. However, these high-performing materials face various challenges, such as the toxicity of lead compounds, which pose significant risks to human health and the environment, and their instability when exposed to moisture and prolonged sunlight [12]. These challenges limit their large-scale industrial applications and commercial viability. Therefore, there is an urgent need to address these challenges to enhance the development and application of these materials.

All inorganic double perovskites with the chemical formula $A_2BB'X_6$ have emerged as promising alternatives to lead-based systems [12]. In these structures, A typically represents a monovalent cation, B is a monovalent metal cation, B' is a trivalent metal cation, and X is an oxygen/halogen anion [12]. The physical properties of these lead-free double perovskites can be tuned by varying their A, B, B', and X compositions [13]. Numerous theoretical and experimental studies have reported different lead-free double perovskite element compositions for diverse applications.

For instance, Alsalari et al. [13] investigated the properties of X_2RbAsI_6 (X = K, Cs) lead-free double perovskites for thermoelectric and optoelectronic applications by using first-principles methods. Their investigation showed that the compounds are semiconductors with wide indirect band gaps of 3.12 eV and 2.14 eV for Cs_2RbAsI_6 and K_2RbAsI_6, respectively. The calculations of the optical properties demonstrated strong absorption in the visible region, while the thermoelectric properties revealed a high figure of merit (ZT) exceeding 0.7, suggesting their potential utility in optoelectronics and thermoelectrics. The properties of $A_2NaMoCl_6$ (A = Cs, Rb) were computed using density functional theory (DFT) [14]. The potential for their utility was confirmed by the negative formation energy. The optical properties revealed significant absorption and low reflectivity in the ultraviolet-visible range, while their ZT exceeded 0.8, indicating their possible applications in thermoelectric and optoelectronic fields. Another study by Qi et al. [15] investigated the photoelectric properties of Cs_2TlBiX_6 (X = Cl, Br, I) using DFT. They found that the compounds displayed excellent structural, mechanical, and thermal stability. Furthermore, they reported high absorption coefficients of 10^5 cm^{-1}, which are suitable for photovoltaic applications. A high value of 25.50% for the spectroscopic limited maximum efficiency was obtained for Cs_2TlBiI_6. Tang et al., studied the properties of the Cs_2InCoX_6(X=F, Cl, Br) perovskite compounds using ab-initio methods [16]. These compounds were found to have direct band gaps of 3.003, 1.129, and 0.365 eV, respectively, and a suitable absorption profile. The $Cs_2InCoCl_6$ compound was found to be the best suited for solar cell applications. The properties of the arsenic-based double perovskite compounds A_2AgAsX_6(A=K, Rb, Cs; X=Cl, Br, I) [17] have been reported using first-principles methods. Among the materials, $K_2AgAsBr_6$ was found to have electronic and optical properties best fit for photovoltaic and photocatalytic applications.

Further theoretical studies have been reported for other element combinations, including Rb_2YCuX_6(X=Br, I) [18], Rb_2CuMF_6 (M = As^{3+}, Bi^{3+}) [19], Dy_2NiMnO_6 [20], Rb_2CuSbZ_6 (Z = F, Br, and I) [21], $K_2CuSbBr_6$ [22], Na_2LiZF_6 (Z = Ir and Rh) [23], Cs_2AgMX_6(M=Co, Rh, Ir; X = Cl, Br, I) [24], Rb_2InSbX_6 (X = F, Cl, Br, I) [25], A_2CuSbX_6 (A = Cs, Rb, K; X = Cl, Br, I) [26], $Cs_2NaB'Cl_6$ (B' = In, Cr, Y, Tb) [27], and Na_2CuMCl_6 (M = Bi, Sb) [28], among others. In addition to theoretical investigations, experimental studies have been conducted on inorganic lead-free double perovskites. A stable $Cs_2AgBiBr_6$ double perovskite material with a power conversion efficiency of 6.37% has been experimentally reported through the hydrogenation method [29]. This represents the highest efficiency reported for any inorganic lead-free double perovskite, which significantly lags behind lead-based perovskites. Therefore, further investigations on lead-free double perovskites are required to bridge this efficiency gap.

Moreover, although previous studies have extensively explored Cl-, Br-, and I-based double perovskites with different elemental combinations, fluoride-based double perovskites with iridium have not been extensively explored. Iridium and fluoro-based compounds have been established to possess stability advantages in the literature [30,31]. This motivated us to investigate the structural, phonon, electronic, elastic, mechanical, thermodynamic, optical, and thermoelectric properties of the novel iridium-fluoride-based double perovskite compound Rb_2NaIrF_6 using DFT. We employed generalised gradient approximation (GGA) and meta-GGA approximations to provide a comprehensive understanding of the properties of this material and its potential for optoelectronic and thermoelectric applications.

2. Computational Methods

The properties of the Rb_2NaIrF_6 lead-free double perovskite compound were computed using a plane wave self-consistent field (Pwscf) basis within density functional theory (DFT) [32] as implemented in the Quantum Espresso (QE) package [33]. The crystallographic information file (CIF) of the studied compound was downloaded from the Materials Project database [34], and its SCF input file was generated using a Quantum Espresso input generator [35]. Scalar relativistic ultrasoft pseudopotentials (USSP) [36] were used in this investigation to compute all the properties, apart from the optical properties, which were computed using norm-conserving pseudopotentials [37]. The generalised gradient approximation (GGA) using Perdew-Burke-Ernzerhof (PBE) [38] and Wu-Cohen (WC) [39] functionals to treat the electron-ion interactions were employed in this study. The GGA tends to underestimate the electronic band gaps of materials being investigated [40,41]. Therefore, the meta-GGA functionals restored-regularised strongly constrained and appropriately normed (r2SCAN) and Tran-Blaha-modified Becke-Johnson (TB-mBJ) [42] were employed to improve accuracy. Other than DFT, the electronic band gaps were further predicted using the Aflow machine learning online tool (AFLOW-ML) accessed at www.aflowlib.org. A converged cutoff energy of 150 Rydberg and a Monkhorst-Pack sampling scheme with a k-point grid optimised at 9 × 9 × 9 with a 1 offset in the first Brillouin zone (BZ) were used for the calculations. The non-self-consistent field (NSCF) calculations were performed using a denser k-point mesh of 12 × 12 × 12. Variable cell relaxation and geometry optimisation of the total energy versus the lattice parameters were conducted using the Broyden-Fletcher-Goldfarb-Shanno (BFGS) algorithm, with convergence thresholds of 10^{-4} Ry and 10^{-3} Ry/Bohr for energy and forces, respectively. The Semi-classical Boltzmann transport theory, which is implemented in the BoltzTraP code [43], was used to compute the thermoelectric properties. BoltzTraP code incorporates the Quantum Espresso output files as input files under the constant relaxation time approximation. A dense k-point mesh of dimensions 15 × 15 × 15 was used to accurately compute the thermoelectric properties. Visualisation of the crystal structure and plotting of the computed and calculated data were performed using VESTA, gnuplot, and Python software.

3. Results and Discussion

3.1 Structural Properties and Stability

The Rb_2NaIrF_6 lead-free double perovskite compound crystallises in a cubic crystal system, space group $Fm\bar{3}m$ (225) [34]. The Rb, Na, Ir and F elements are located at (1/4, 3/4, 3/4), (1/2, 0, 0), (0, 0, 0) and (1/2, 0, 0.734992) coordinates, respectively, with the corresponding Wyckoff sites at 8c, 4b, 4a, and 24e. The crystal structure features bond lengths of 3.07 Å for Rb-F, 2.30 Å for Na-F, and 2.04 Å for Ir-F, respectively. The cubic crystal structure of the Rb_2NaIrF_6 lead-free double perovskite compound is shown in Fig. 1.

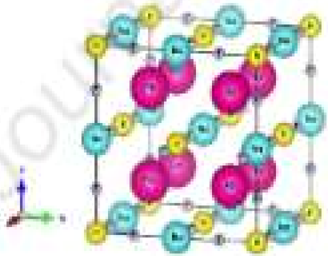

Fig. 1. Crystal structure of the Rb_2NaIrF_6 lead-free double perovskite compound.

Geometry optimisation is performed by computing the total energy as a function of volume and fitting the values to the Birch-Murnaghan equation of state (equation (1)) [44] to obtain the optimised ground-state structural parameters.

$$E(V) = E_0 + \frac{B}{B'(B'-1)}\left[V\left(\frac{V_0}{V}\right)^{B'} - V_0\right] + \frac{B}{B'}(V - V_0) \tag{1}$$

Where E_0, B, B', V, and V_0 refer to the minimum total energy, bulk modulus, first pressure derivative of the bulk modulus, total unit cell volume, and ground state unit cell volume, respectively.

Fig. 2 depicts the Birch-Murnaghan equation of state fit plot of the total energy versus volumes of the Rb_2NaIrF_6 lead-free double perovskite compound. The obtained ground-state total minimum energies, lattice parameters, and volumes are listed in Table 1. The optimised lattice parameter and volume are obtained as 16.45 a.u and 4451.54 a.u^3, which are consistent with the values reported in the Materials Project database [45]. This demonstrates the accuracy of our calculations for predicting the structural properties. There is no direct experimental work on the synthesis of Rb_2NaIrF_6 lead-free double perovskite compound for comparison and validation of its structural properties; hence, there is a need for future experimental work to confirm the obtained theoretical predictions.

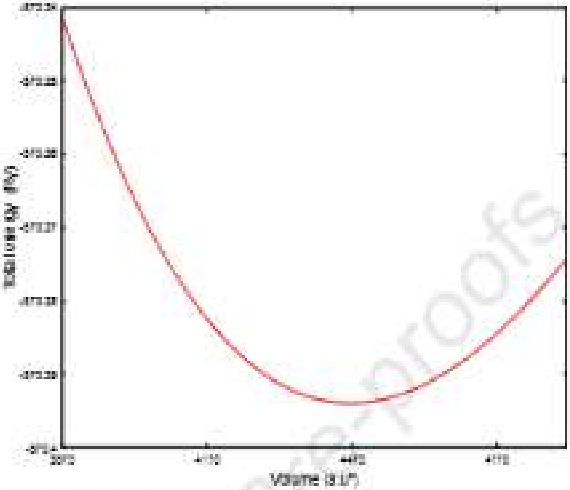

Fig. 2. Birch-Murnaghan equation of state fit plots of the Rb_2NaIrF_6 lead-free double perovskite compound.

Table 1. Structural properties of Rb_2NaIrF_6 lead-free double perovskite compound.

	GGA-PBE	Other works [45]
Equilibrium Energy E_0 (Ry)	-670.29	
Lattice parameter a_0 (a.u)	16.45	16.44
Equilibrium volume V_0 (a.u³)	4451.54	4435.15
τ_G	0.99	
μ	0.64	

Energy of formation ΔH_f (Ry)	-1.67

The Goldschmidt tolerance factor (t_G) and octahedral factor (μ) were used to establish the structural stability of the perovskite material [46]. These are given by equations (2) and (3) [46].

$$t_G = \frac{R_A + R_X}{\sqrt{2}(R_B + R_X)} \quad (2)$$

$$\mu = \frac{R_B}{R_X} \quad (3)$$

Where r_A, r_B, and r_X are the Shannon ionic radii of the A and B cations and the X anions, respectively. For double perovskites, r_B is the average ionic radius of the B and B' cations. A structure is termed a stable cubic perovskite structure if the Goldschmidt tolerance factor limit is within $0.8 < t < 1$ and the octahedral factor $\mu > 0.425$ [47]. As presented in Table 1, the obtained Goldschmidt tolerance and the octahedral factors for the Rb_2NaIrF_6 crystal structure are 0.99 and 0.64, respectively, suggesting structural stability. The energy of formation (ΔH_f) of a compound is the amount of energy released or absorbed when the compound is created from individual elements [48]. The thermodynamic stability was demonstrated by calculating the ΔH_f from equation (4) [46].

$$\Delta H_f = E_{Rb_2NaIrF_6} - (2E_{Rb} + E_{Na} + E_{Ir} + 6E_F)$$
(4)

$E_{Rb_2NaIrF_6}$ refers to the total energy of the Rb_2NaIrF_6 compound, whereas E_{Rb}, E_{Na}, E_{Ir}, and E_F are the total energies of the individual Rb, Na, Ir, and F atoms, respectively.

The ΔH_f value was calculated to be -1.67, as presented in Table 1. The negative ΔH_f implies that the Rb_2NaIrF_6 lead-free double perovskite compound is thermodynamically stable and can be experimentally synthesised [45]. The phonon properties are significant in determining the dynamic stability of materials. Fig. 3 shows the obtained phonon dispersion curve of the Rb_2NaIrF_6 lead-free double perovskite compound. It was observed that the phonon scattering frequencies were above zero, and no imaginary frequency modes were observed. This indicates the dynamic stability of the studied compound; hence, it can be potentially synthesised experimentally.

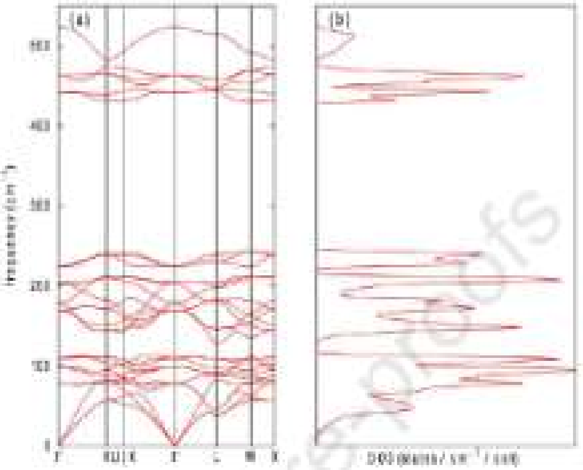

Fig. 3. GGA-PBE (a) phonon dispersion and (b) density of states curves of Rb_2NaIrF_6 lead-free double perovskite compound.

3.2 Electronic Properties

The electronic properties of a material are crucial for determining its potential application in devices. Fig. 4 depicts the electronic band structure and projected density of states of the material under study, utilising the GGA-PBE approximation as a representative GGA method. The separation gap between the valence and conduction bands suggested a semiconducting nature. The valence band maxima and conduction band minima are located at the same symmetry point (X-X) of the first Brillouin zone, implying that the compound under study is a direct band gap semiconductor. The band gaps obtained using GGA-PBE and GGA-WC approximations are 2.20 and 2.14 eV. These wide band gaps correspond to the UV absorption, implying that the material can be used as a UV light absorber in optoelectronic device applications. From the projected density of states results, the formation of the valence band was found to be a result of the hybridisation of the Ir3d, Ir2p, and F2p orbitals. In contrast, the formation of the conduction band was found to be a result of the hybridisation of the Rb2s, Rb4p, Na2s, Ir1s, Ir2p, Ir3d, and F2p orbitals. Since the GGA approximation tends to underestimate the electronic band gaps of materials [40,41], the meta-GGA approximations were used to improve the accuracy of the GGA band gaps. Fig. 5 shows the TB-mBJ band structure and density of states as a representative. Table 2 shows that the band gaps improved to 2.78 and 3.76 eV using R2SCAN and TB-mBJ approximations. In addition to DFT, the ML technique was utilised to predict the band gap, which was obtained as 2.33 eV. This close band gap to the GGA band gaps indicates the accuracy of our DFT methods in predicting electronic band gaps. The reported GGA band gaps agree with the band gap (2.40 eV) reported in the Materials Project Database.

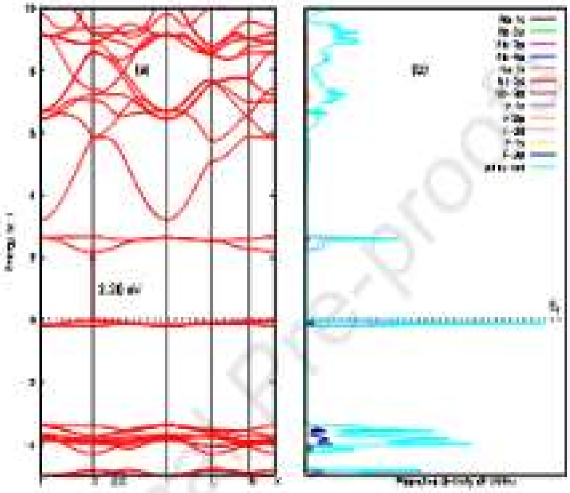

Fig. 4. The GGA-PBE (a) electronic band structure and (b) projected density of states of Rb_2NaIrF_6 lead-free double perovskite compound.

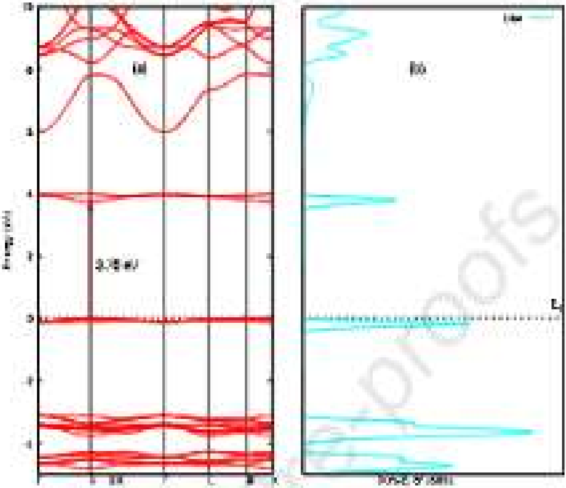

Fig. 5. The TB-mBJ (a) electronic band structure and (b) density of states of the Rb_2NaIrF_6 lead-free double perovskite compound.

Table 2. The electronic band gaps of the Rb_2NaIrF_6 lead-free double perovskite compound calculated using different approximations.

Methods	Band gaps (eV)
GGA-PBE	2.20
GGA-WC	2.14
R2SCAN	2.78
TB-mBJ	3.76

ML	2.33
Other works [34]	2.40

3.3 *Elastic and Mechanical Properties*

The Rb_2NaIrF_6 lead-free double perovskite compound adopts a cubic crystal system with the Fm3̄m [225] space group. The cubic crystal system features three independent elastic constants: C_{11}, C_{12}, and C_{44} [50]. The elastic stability criteria for the cubic crystal system are given by equation (5) [50].

$$C_{11} - C_{12} > 0,\ C_{11} + 2C_{12} > 0,\ C_{44} > 0 \tag{5}$$

The elastic constants for the Rb_2NaIrF_6 lead-free double perovskite compound presented in Table 3 conform to equation (5), suggesting mechanical stability. The mechanical properties of Rb_2NaIrF_6 lead-free double perovskite compound, including the bulk modulus B, Young's modulus E, Shear modulus G, and Poisson's ratio ν, were deduced from the elastic constants according to the Voigt-Reuss-Hill approximation, as presented in Table 4. The ability of Rb_2NaIrF_6 lead-free double perovskite compound to resist volume deformation, uniaxial tension, and plastic deformation is described by B, E, and G, respectively [51]. The studied compound portrays the behaviour of a soft and less stiff material due to its low B, G, and E values. Pugh's and Poisson's ratios (B/G and ν) describe the ductile/brittle behaviour of the materials. A material is termed ductile if B/G > 1.75, otherwise, it is brittle [52]. Furthermore, an ν > 0.26 suggests ductile character, otherwise, it is brittle [52]. As observed in Table 4, the Rb_2NaIrF_6 lead-free double perovskite compound exhibited ductile behaviour. The Poisson's ratio can also describe the nature of bonding within materials. A value of ν ~ 0.25 implies an ionic nature [53]. Based on this criterion, the studied compound was determined to be an ionic crystal.

Table 3. Elastic tensor (C_{ij}) in GPa for the Rb_2NaIrF_6 cubic crystal structure.

	C_{11}	C_{12}	C_{44}
GGA-PBE	71.36	21.97	15.93

Table 4. Computed mechanical properties: bulk modulus B, Young's modulus E, Shear modulus G, Pugh's ratio B/G, Poisson's ratio n, Anisotropy factor A, Debye velocity V_m, and Debye temperature θ_D of Rb_2NaIrF_6 lead-free double perovskite compound.

	B	E	G	B/G	n	A	V_m(m/s)	θ_D(K)
GGA-PBE	38.43	48.97	19.02	2.02	0.28	0.65	2158.45	252.47

The anisotropy factor measures the degree of anisotropy in a material. The anisotropy factor is expressed in the form of equation (5) [54].

$$A = \frac{2C_{44}}{C_{11}-C_{12}} \tag{5}$$

When the A value is 1, the material under investigation is considered isotropic, whereas a deviation from this value indicates the degree of anisotropy in the material [55]. The calculated A value of 0.65 indicates that the Rb_2NaIrF_6 lead-free double perovskite compound is highly anisotropic. Furthermore, the mechanical anisotropic behaviour of the Rb_2NaIrF_6 lead-free double perovskite compound was studied from the computed elastic constants using the ELATE: Elastic matrix tensor analysis [56] software. The 2D spatial dependence maps of Young's modulus, Shear modulus, and Poisson's ratio in the xy, xz, and yz planes are shown in Fig. 6(a-c). The coloured lines in the spatial dependence maps represent the measure of anisotropy. The degree of the curvature of the coloured lines indicates the magnitude of anisotropy [49]. The degree of the anisotropy increases with the curvature of the coloured lines towards the centre of the circle and decreases with the curvature of the coloured lines towards forming a complete circle [49] . Based on the spatial dependence maps in Fig. 6, the Shear modulus and Poisson's ratio maps in the xy, xz, and yz planes showed high anisotropy, corroborating the anisotropy factor value.

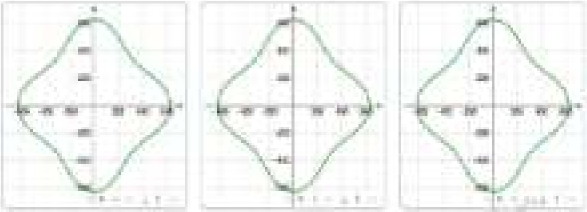

(a) Young's modulus in xy Young's modulus in xz Young's modulus in yz

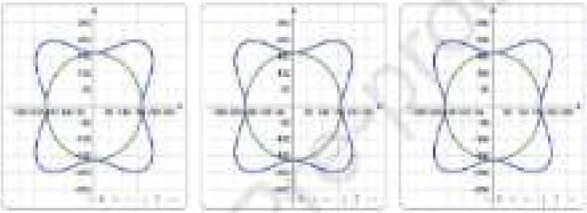

(b) Shear modulus in xy Shear modulus in xz Shear modulus in yz

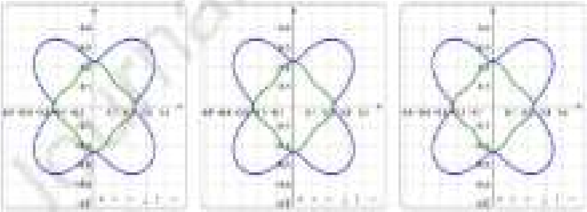

(c) Poissons Ratio in xy Poissons Ratio in xz Poissons Ratio in yz

Fig. 6. Two-dimensional spatial dependence maps of (a)Young's modulus, (b) shear modulus, and (c) Poisson's ratio of the Rb_2NaInF_6 lead-free double perovskite compound.

The Debye temperature (θ_D) is a thermodynamic property that provides insights into the atomic vibration patterns in a crystal [46] and is expressed in the form of equation (7) [57].

$$\theta_D = \frac{h}{k}\left[\frac{3n}{4\pi}\left(\frac{N_A \rho}{M}\right)\right]^{1/3} v_m \tag{7}$$

Where h, k, n, N_A, ρ, and M refer to Planck's constant, Boltzmann's constant, the number of atoms, Avogadro's constant, charge density, and molecular weight, respectively. In this study, θ_D was obtained as 282.47 K. The Debye temperature is related to other thermodynamic properties, including the vibrational energy, vibrational free energy, entropy, and heat capacity, as discussed in the next section.

3.4 Thermodynamic Properties

The changes in the Debye vibrational energy, vibrational free energy, entropy, and heat capacity with temperature are shown in Fig. 7(a-d). The vibrational energy of the system increased linearly with the temperature (Fig. 7(a)). In contrast, the vibrational free energy follows the fitting algorithm for exponential decay, as shown in Fig. 7(b). The vibrational free energy curve further indicates that the Rb_2NaInF_6 lead-free double perovskite compound is thermodynamically stable between 0 and 200 K with positive values. Entropy is a physical parameter that describes the degree of disorder in a material [58]. Fig. 7(c) shows that the entropy curve increases exponentially as the temperature increases. This is because an increase in temperature increases the thermal motion of the molecules within the material, which increases the degree of disorder of the molecules [58]. The highest entropy value of 610 K was achieved for the Rb_2NaInF_6 lead-free double perovskite compound at 800 K. The heat capacity describes a material's ability to store heat [59], and it constitutes contributions from both lattice vibrations and electron motion. Fig. 7(d) shows that the heat capacity of Rb_2NaInF_6 sharply increased at 0 – 300 K, which is consistent with the Debye model ($C_v \propto T^3$) law [58]. For temperatures up to 500 K, most of the low-energy vibration modes were thermally excited. Beyond 500 K, the heat capacity plateaus, and a further temperature rise does not result in a significant change, which conforms to the Dulong-Petit law for all solids [59].

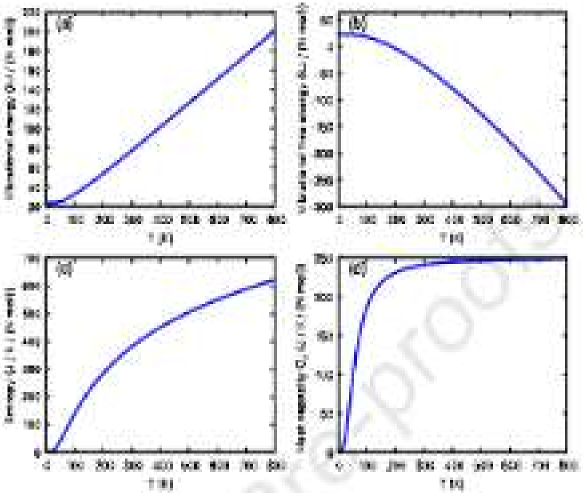

Fig. 7. Thermodynamic properties of Rb_2KAlF_6 lead-free double perovskite compound: (a) vibrational energy, (b) vibrational free energy, (c) entropy, and (d) heat capacity as a function of temperature.

3.5 Optical Properties

The optical characterisation of materials is desirable to establish their viability for optoelectronic applications. The electron response in a material is characterised by a complex dielectric wave function [60,61] , which is represented by equation (5).

$$\varepsilon(\omega) = \varepsilon_1(\omega) + i\varepsilon_2(\omega) \quad (5)$$

Here, $\varepsilon_1(\omega)$ and $\varepsilon_2(\omega)$ refer to the real and imaginary parts of the complex dielectric wave function, respectively. Other optical properties, such as the absorption coefficient $\alpha(\omega)$, refractive index $n(\omega)$, extinction coefficient $K(\omega)$, reflectivity $R(\omega)$, and energy loss function $L(\omega)$, were computed using equations (6) to (12) [62–65].

$$\alpha(\omega) = \sqrt{2}\omega\left(\sqrt{\varepsilon_1^2(\omega) + \varepsilon_2^2(\omega)} - \varepsilon_1(\omega)\right)^{1/2} \quad (6)$$

$$n(\omega) = \left(\frac{\sqrt{\varepsilon_1^2(\omega)+\varepsilon_2^2(\omega)}+\varepsilon_1(\omega)}{2}\right)^{1/2} \tag{10}$$

$$K(\omega) = \left(\frac{\sqrt{\varepsilon_1^2(\omega)+\varepsilon_2^2(\omega)}-\varepsilon_1(\omega)}{2}\right)^{1/2} \tag{11}$$

$$L(\omega) = \frac{\varepsilon_2(\omega)}{\varepsilon_1^2(\omega)+\varepsilon_2^2(\omega)} \tag{12}$$

$$R(\omega) = \frac{(n-1)^2+k^2}{(n+1)^2+k^2} \tag{13}$$

The optical properties of Rb_2NaIrF_6 were computed across a photon energy range of 0-15 eV, as shown in Fig. 8(a-d). The real part of the dielectric constant describes the electron polarisation within a material [56]. The $\varepsilon_1(\omega)$ in Fig. 8(a) starts at approximately 2.92 at 0 eV and exhibits a gradual increase with energy, reaching a peak around 6-7 eV. Thereafter, $\varepsilon_1(\omega)$ decreases and attains negative values between 7.8-8.1 eV, symbolising the attenuation of the propagation of photons within the Rb_2NaIrF_6 [46]. This negative zone signifies a transition from dielectric to metallic character [46]. Finally, the $\varepsilon_1(\omega)$ increases with increasing energy, suggesting a restoration of dielectric character. The $\varepsilon_2(\omega)$ describes the material's ability to dissipate energy [57]. The visible peaks of the $\varepsilon_2(\omega)$ in Fig. 8(a) indicate an ultraviolet interband transition from the valence to the conduction band. The $\varepsilon_2(\omega)$ curve remains low near zero at low energies, but increases significantly beyond 2 eV, indicating the onset of optical absorption due to direct electronic transitions. This onset corresponds to the electronic band gap value obtained using the GGA-PBE approximation. A sharp peak in $\varepsilon_2(\omega)$ was observed near 6-8 eV, suggesting a strong absorption in this energy region.

The $n(\omega)$ describes the transparency of a material [47]. Fig. 8(b) shows that the static refractive index $n(0)$ of Rb_2NaIrF_6 is 1.71. The $n(\omega)$ curve starts at $n(0)$, it increases with increasing photon energy, attaining a maximum of 2.91 at 7 eV, and thereafter gradually decreases as the photon energy increases, suggesting a dispersive optical response in the visible and UV regions. A refractive index value above 1 indicates the semiconducting nature of the studied material [68]. Additionally, the high $n(\omega)$ in the ultraviolet-visible regime suggests the low transparency of Rb_2NaIrF_6, hence, high light absorption potential within this regime [47]. The $K(\omega)$ describes the attenuation of the incident light by a material [69]. Fig. 8(b) shows that the $K(\omega)$ curve remains low at low photon energies and begins to increase significantly above 2 eV. The peak near 6-8 eV corresponds to high absorption, in agreement with the behaviour of $\varepsilon_2(\omega)$. The $\alpha(\omega)$ describes the material's potential to capture photons of specific energy [70]. The $\alpha(\omega)$ curve in Fig. 8(c) is nearly zero in the infrared and visible range (0-2 eV), indicating transparency at low energies. However, a steep increase occurs beyond 3 eV, reaching its highest values between 6 and 10 eV, where strong absorption dominates due to interband transitions. The high absorption coefficient of Rb_2NaIrF_6 makes it an efficient UV-light absorber.

The R(ω) is an important optical parameter that describes a material's surface behaviour [70]. Fig. 9(d) shows that the R(ω) remains relatively low at lower energies, but increases significantly at higher energies. An increase above 6 eV indicates enhanced reflection in the UV region, which is associated with high-energy electronic excitations. The increasing reflectivity at high energies suggests the potential of Rb_2NaIrF_6 for applications in UV-reflective coatings [66]. The L(ω) represents the energy dissipation of an electromagnetic wave within the material and is closely related to electron energy loss [71]. It is typically dominated by plasmon resonances and peaks where the $\varepsilon_1(\omega)$ approaches zero [71]. For Rb_2NaIrF_6, L(ω) is expected to exhibit prominent peaks in the UV range, particularly around the energy region where $\varepsilon_1(\omega)$ crosses zero. These peaks indicate strong energy dissipation mechanisms, which are crucial for understanding the plasmonic response of the material. Fig. 9(d) shows a low-loss window in the infrared and visible ranges, making Rb_2NaIrF_6 a suitable candidate for applications requiring transparency in these regions. The high absorption in the UV range indicates strong interband transitions, which could be relevant for UV optoelectronics [72,73] and photovoltaic applications. Our optical properties corroborate those reported for other lead-free double perovskites with similar stoichiometry [74].

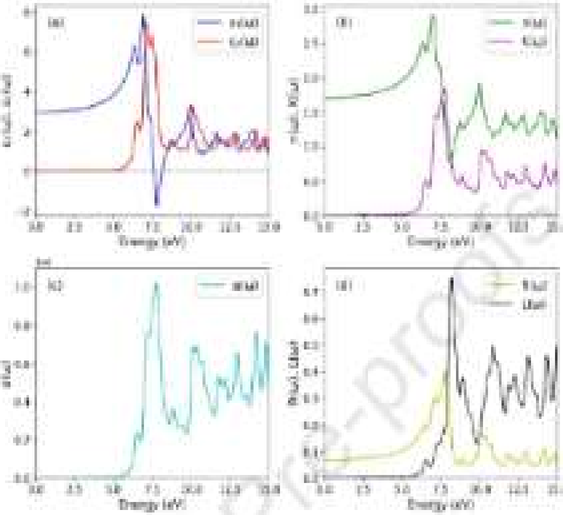

Fig. 8. The optical properties of the Rb_2NaIrF_6 lead-free double perovskite compound computed using the GGA-PBE approximation. (a) $\varepsilon_1(\omega)$ and $\varepsilon_2(\omega)$, (b) $n(\omega)$ and $K(\omega)$, (c) $\alpha(\omega)$, and (d) $R(\omega)$ and $L(\omega)$.

3.6 Thermoelectric Properties

The thermoelectric properties, including the Seebeck coefficient (S), electrical conductivity (σ/τ), and electronic thermal conductivity (k_e/τ) of Rb_2NaIrF_6 across the temperature (T) range of 200-1000 K, were computed using the BoltzTrap code as shown in Fig. 9(a-c). The S in Fig. 9(a) demonstrates negative values throughout the 200-1000 K range, implying n-type semiconductor behaviour [75]. The S increases from -241.21 μV/K at 200 K to -174.66 μV/K at 1000 K, a characteristic semiconductor behavior [76]. Electrical conductivity describes the ability of a material to conduct electrical current [77]. In semiconductors, the valence and conduction bands are well separated by the band gap. An increase in temperature gives electrons sufficient energy to move from the valence band to the conduction band. The mobility of free electrons contributes to the electrical conductivity of semiconductor materials [78]. Fig. 9(b) shows the effect of temperature on the electrical conductivity σ/τ in the Rb_2NaIrF_6 double perovskite compound. A remarkable temperature dependence of the σ/τ is observed in Fig. 9(b), which increases from 1.14×10^{18} $(\Omega ms)^{-1}$ at 200 K to 7.76×10^{18} $(\Omega ms)^{-1}$ at 1000 K. This significant increase indicates thermally activated charge transport mechanisms, likely resulting from the increased electron concentration and enhanced electron mobility at elevated temperatures. The electrical conductivity (σ) is related to the charge carrier concentration (n), according to equation 14 [58].

$$\sigma = ne\mu \tag{14}$$

Where e is the electron charge and μ is the mobility of the charge carriers. Thermal conductivity constitutes the electronic (κe) and lattice (κl) thermal contributions. The κe results from charge carrier mobility, whereas κl results from phonons [79]. The electronic thermal conductivity κe/τ depicted in Fig. 9(c) increases from 1.75×10^{14} W/m·K·s at 200 K to 2.91×10^{14} W/m·K·s at 1000 K. This increase follows the Wiedemann–Franz law [80], which predicts that the electronic thermal conductivity scales with electrical conductivity and temperature. The electronic thermal conductivity was lower than the electrical conductivity, suggesting the high thermoelectric performance of the Rb_2NaInF_6 material. The increasing electronic contribution to the thermal transport becomes increasingly dominant at higher temperatures. The power factor PF ($S^2\sigma$) [78] shown in Fig. 9(d) increases from 5.62×10^{10} W/m K^2·s at 200 K to a maximum of 2.45×10^{11} W/m·K^2·s at 800 K before slightly decreasing to 2.37×10^{11} W/m K^2·s at 1000 K. This trend identifies an optimal operating temperature window of approximately 800–850 K, where the tradeoff between increasing Seebeck coefficient and electrical conductivity yields the maximum PF. Because the lattice vibrations do not fall within the scope of the BoltzTrap algorithm, the lattice thermal conductivity κl was computed using the phonopy module [81] alongside Quantum Espresso software [33]. Fig. 9(e) shows that κl decreases from 8.93×10^{8} W/m K.s at 200 K to 2.26×10^{8} W/m K.s at 1000 K. This significant decrease results from the enhanced phonon-phonon scattering at elevated temperatures [82]. Lattice thermal conduction is significantly lower compared to electronic thermal conduction. The low lattice thermal conductivity at high temperatures is particularly beneficial for thermoelectric performance because it helps maintain the temperature gradients necessary for efficient thermoelectric conversion. The thermoelectric figure of merit, ZT, was calculated from the computed thermoelectric properties according to equation (15) [83].

$$ZT = \frac{S^2\sigma T}{\kappa_e + \kappa_l} \tag{15}$$

Fig. 9(f) shows a steady improvement of ZT across the temperature range, increasing from 0.76 at 200 K to 0.81 at 1000 K. Notably, ZT exceeds 0.80 from 750 K onward, reaching a peak value of 0.81 at 1000 K. The continuous improvement in ZT demonstrates how increasing the Seebeck coefficient and electrical conductivity, and decreasing the lattice thermal conductivity, favourably impact the overall thermoelectric performance at higher temperatures. The relatively high and stable ZT values throughout the operating temperature range 750 K to 1000 K suggest that Rb_2NaInF_6 is a promising candidate for mid- and high-temperature thermoelectric applications. These applications include industrial waste heat recovery systems operating at high temperatures, high-temperature solar thermal energy conversion, and power generation in extreme environments [84]. The trend of the thermoelectric properties obtained in this work closely matches that reported in the literature [85] for all-inorganic lead-free double perovskites.

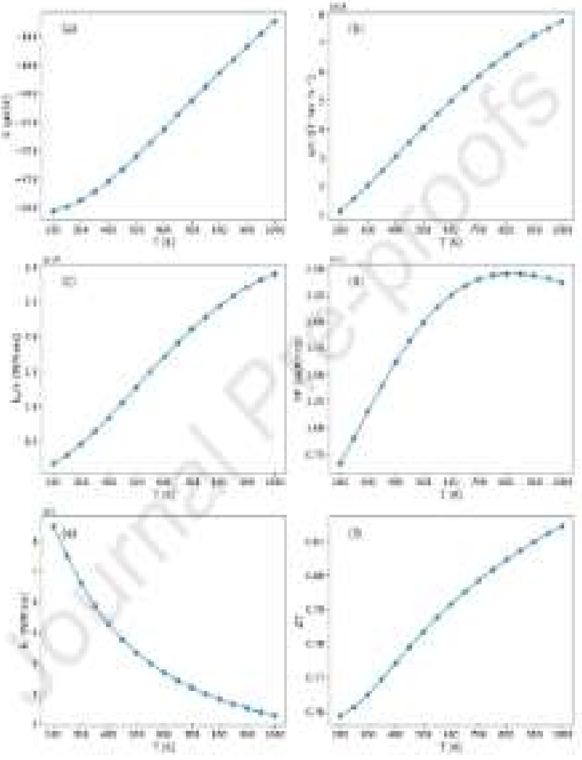

Fig. 9. The thermoelectric properties of the Rb_2NaInF_6 lead-free double perovskite compound. (a) Seebeck coefficient (S), (b) Electrical conductivity (σ/τ), (c) Electronic thermal conductivity (κ_e/τ), (d) Power factor (PF), (e) Lattice thermal conductivity (κ_L), and (f) Figure of merit (ZT).

4. Conclusion

In summary, the structural, electronic, elastic, thermodynamic, optical, and thermoelectric properties of Rb_2NaIrF_6 lead-free double perovskite compound were studied using first-principles methods. Our structural calculations proved the Rb_2NaIrF_6 compounds' structural stability by a Goldschmidt tolerance and the octahedral factors of 0.99 and 0.64, respectively. Thermodynamic stability was established by negative formation energies of -1.67 Ry and positive frequency modes of the phonon dispersion curves. The Rb_2NaIrF_6 compound exhibits a semiconducting nature with band gaps ranging from 2.14 to 3.75 eV, as determined by various computational methods and machine learning tools. The valence band was found to result from the hybridisation of the Ir3d, Ir2p, and F2p orbitals, whereas the conduction band was found to form as a result of the hybridisation of the Rb2s, Rb4p, Na2s, Ir1s, Ir2p, Ir3d, and F2p orbitals. The Born-Huang criterion proved the mechanical stability. The mechanical properties confirmed the ductile, ionic, and anisotropic nature of the Rb_2NaIrF_6 compound. The optical properties revealed high absorption coefficients in the ultraviolet (UV) region (6-10 eV), suggesting the suitability of the Rb_2NaIrF_6 compound for UV optoelectronic device applications. In addition, the high thermoelectric figure of merit (0.81 at T > 900 K) proves that the Rb_2NaIrF_6 lead-free double perovskite compound is an excellent thermoelectric material for heat-to-electrical energy conversion. The limitation of the Rb_2NaIrF_6 compound is the poor absorption of photons in the visible light region, which hinders its application as an absorber in energy devices, such as solar cells. Future research studies should explore the effects of doping as a strategy to tune the optoelectronic properties of the Rb_2NaIrF_6 compound. Overall, this study provides a theoretical basis for the potential applications of Rb_2NaIrF_6 in optoelectronics and thermoelectrics, as well as new guidance for the future synthesis and determination of lattice parameters, band gaps, and absorption behaviour using experiments.

Declaration of Competing Interest

The authors declare no known competing interests that may have influenced this work.

Credit Authorship Contribution Statement

Mwende Mbilo: Funding acquisition, Project administration, Conceptualization, Methodology, Investigation, Formal analysis, Data curation, Validation, Writing – review and editing. **Robinson Musembi**: Computational resources, Methodology, Investigation, Formal analysis, Data curation, Validation, Writing – review and editing. **John Peter Kachira**: Methodology, Investigation, Formal analysis, Data curation, Writing – review and editing. **Wiley Nyangau Onsase**: Methodology, Investigation, Formal analysis, Data curation, Writing – review and editing. **Fanuel Mugwanga Keheze**: Methodology, Investigation, Formal analysis, Data curation, Writing – review and editing. **Refilwe Edwin Mapasha**: Computational resources, Methodology, Investigation, Formal analysis, Data curation, Writing – review and editing.

Data Availability

Data will be provided upon reasonable request.

Acknowledgements

The work was carried out with the financial support of the World Bank under the project "Africa Regional Scholarship and Innovation Fund for Applied Sciences, Engineering and Technology (RSIF)", financed under P165581 IDA D3470, TF A8639, and TDF B1033. The views expressed herein do not necessarily reflect the official opinions of the donors. The authors acknowledge the University of Nairobi for resources in doing this work and the Centre for High-Performance Computing (CHPC-RSA) for computing resources through the account number MATS1321. REM is grateful to the University of Pretoria for the availability of financial support.

References

[1] Ou T, Zhuang Q, Yan H, Feng S, Li P, Ma X. Lead-free halide double perovskites Rb2InSbX6 (X = F, Cl, Br, I): A first-principles study of structural and optoelectrical properties. Chem Phys. 2023;573:112015. https://doi.org/10.1016/j.chemphys.2023.112015.

[2] Alsuhaibani AM, Amina, Rahman F, Liaqat M, Quraishi AM, Norberdiyeva M, et al. High thermoelectric and opto-electronic properties of Ba3NX3 (X=F, Cl) perovskite: insights from DFT computation. Radiat Phys Chem. 2024;225:112129. https://doi.org/10.1016/j.radphyschem.2024.112129.

[3] Alsuhaibani AM, Kamran M, Rehman F, Elhadi M, Khan I, Tirth V, et al. First-principle Insight into Structural, Electronic, Optical and Elastic Properties of AgXF3 (Cr, Zr) Halide Perovskite Materials for Application of Reflective Coating. J Inorg Organomet Polym Mater. 2024;34:3613-3622. https://doi.org/10.1007/s10904-024-03036-1.

[4] Ahmed N, Arif A, Khan S, Mukhtar S, Nasim MH, Rahman F, et al. Experimental and theoretical study of electronic, magnetic and mechanical properties ofCubic LaMnO3 under extreme stress. Mater Res Express. 2020;6:126123. https://dx.doi.org/10.1088/2053-1591/ab5a84.

[5] Ennassiri N, Tahiri N, El Bounagui O, Ez-Zahraouy H, Benyoussef A. Magnetic, magnetocaloric and transport properties in AlCMn3 antiperovskite compound. J Alloys Compd. 2018;741:1195–1202. https://doi.org/10.1016/j.jallcom.2018.01.223.

[6] Dahbi S, Tahiri N, El Bounagui O, Ez-Zahraouy H. Chalcogens' impurities and a single F-center in perovskite SrHfO3 compound: Ab initio calculations. Mater Sci Semicond Process. 2022;138:106271.

https://doi.org/10.1016/j.mssp.2021.106271.

[7] Ali AH, Kadhim AA, Abdulhussain AA, Abed WA, Kadhim KF, Nattiq MA, et al. Computational study of half-metallic behavior, optoelectronic and thermoelectric properties of new XAlN3 (X = K, Rb, Cs) perovskite materials. J Phys Chem Solids. 2024;188:111899. https://doi.org/10.1016/j.jpcs.2024.111899.

[8] Shahzad MK, Hussain S, Riaz M, Sattar H, Ashraf GA, Azeem W, et al. Investigation of ultra wide bandgap Flouro-perovskite materials RBeF3 (R=K and Li) for smart window applications: A DFT study. Heliyon. 2024;10:e29143. https://doi.org/10.1016/j.heliyon.2024.e29143.

[9] Asiri AM, Shahzad MK, Hussain S, Zhu K, Khan SB, Alamry KA, et al. Analysis of XGaO3 (X = Ba and Cs) cubic based perovskite materials for photocatalytic water splitting applications: a DFT study. Heliyon. 2023;9:e14112. https://doi.org/10.1016/j.heliyon.2023.e14112.

[10] Shahzad MK, Farooq MU, Laghari RA, Khan MA, Tahir MB, Azeem W, et al. Investigation of structural, electronic, mechanical, & optical characteristics of Ra based-cubic hydrides RbRaX3 (X= F and Cl) perovskite materials for solar cell applications: First principle study. Heliyon. 2023;9:e18407. https://doi.org/10.1016/j.heliyon.2023.e18407.

[11] Green MA, Dunlop ED, Yoshita M, Kopidakis N, Bothe K, Siefer G, et al. Solar cell efficiency tables (Version 63). Prog Photovoltaics Res Appl. 2024;32:3–13. https://doi.org/10.1002/pip.3750.

[12] Roknuzzaman M, Alarco JA, Wang H, Ostrikov K (Ken). Structural, electronic and optical properties of lead-free antimony-copper based hybrid double perovskites for photovoltaics and optoelectronics by first principles calculations. Comput Mater Sci. 2021;186:110009. https://doi.org/10.1016/j.commatsci.2020.110009.

[13] Tang T, Tang Y. First principle comparative study of transitional elements Co, Rh, Ir(III)-based double halide perovskites. Mater Today Commun. 2023;34:105431. https://doi.org/10.1016/j.mtcomm.2023.105431.

[14] El-marghany A, Muhammad K, Sajid M, Nazar M, Kashif Masood M, Nasarullah, et al. Unraveling the complexities of A2NaMoCl6 (A=Cs, Rb) halide double perovskites through theoretical methods. J Phys Chem Solids. 2025;198:112477. https://doi.org/10.1016/j.jpcs.2024.112477.

[15] Qi F, Fu X, Meng L, Lu C-Z. Exploring High–Performance All-Inorganic perovskite materials for Next-Generation photovoltaic Applications: A theoretical study on Cs2TiBiX6 (X = Cl, Br, I). Comput Theor Chem. 2024;1233:114500. https://doi.org/10.1016/j.comptc.2024.114500.

[16] Tang TY, Zhao XH, Hu DY, Liang QQ, Wei XN, Tang YL. An ab-initio investigation of novel double halide perovskite Cs2InCoX6(X=F, Cl, Br) materials with direct band structure and broadband light absorption. Mater Sci

Semicond Process. 2022;152:107047. https://doi.org/10.1016/j.mssp.2022.107047.

[17] Tang T, Tang Y. A first principle comparison of arsenic-based double halide perovskite materials for photovoltaic and optoelectronic application. J Solid State Chem. 2022;316:123557. https://doi.org/10.1016/j.jssc.2022.123557.

[18] Rehman F, Amina, Elboughdiri N, Shermazarov I, Quraishi AM, Mohsen Q, et al. Exploring the structural, electronic, optical, mechanical and thermoelectric properties of copper based double perovskites Rb_2YCuX_6 (X=Br, I). J Phys Chem Solids. 2025;196:112382. https://doi.org/10.1016/j.jpcs.2024.112382.

[19] Boutramine A, Al-Qaisi S, Samah S, Alqorashi AK, Alrebdi TA, Ezzeldien M, et al. First-principles Investigations of Structural, Thermodynamic, Optoelectronic and Thermoelectric Properties of Rb_2CuMF_6 ($M = As^{3+}, Sb^{3+}$) Eco-friendly Halide Double Perovskites: Materials for Green Energy Applications. J Inorg Organomet Polym Mater. 2024;34:4133–4145. https://doi.org/10.1007/s10904-024-03124-1.

[20] Shahadath N, Siddique MAB, Tarekuzzaman M, Ishraq MH, Rahman MF, Arif AM, et al. Optimization of high efficiency lead-free double perovskite Dy_2NiMnO_6 (DNMO) for optimal solar cell and renewable energy applications: a numerical SCAPS-1D simulation. New J Chem. 2024;48:14336–14353. https://doi.org/10.1039/D4NJ02784J.

[21] Al-Qaisi S, Iram N, Boutramine A, Alqorashi AK, Alrebdi TA, Rached H, et al. Theoretical Investigation of a new Double Perovskites of Rb_2CuSbZ_6 (Z = F, Br, and I) for Sustainable Technologies. J Inorg Organomet Polym Mater. 2024;34:6146–6158. https://doi.org/10.1007/s10904-024-03250-w.

[22] Ferdous Rahman M, Gebo T Al, Amami M, Farhat L Ben. Exploring the structural, optical, electronic, and mechanical characteristics of the novel inorganic lead-free double perovskite $K_2CuSbBr_6$ for advanced optoelectronic devices. Polyhedron. 2025;274:117513. https://doi.org/10.1016/j.poly.2025.117513.

[23] Es-Smairi A, Al-Qaisi S, Sfina N, Boutramine A, Jappor HR, Alzahrani HS, et al. DFT Insights Into the Structural, Stability, Elastic, and Optoelectronic Characteristics of Na_2LiZF_6 (Z = Ir and Rh) Double Perovskites for Sustainable Energy. J Comput Chem. 2025;46: e70097. https://doi.org/10.1002/jcc.70097.

[24] Tang T, Tang Y. First principle comparative study of transitional elements Co, Rh, Ir(III)-based double halide perovskites. Mater Today Commun. 2023;34:105431. https://doi.org/10.1016/j.mtcomm.2023.105431.

[25] Ou T, Zhuang Q, Yan H, Feng S, Li P, Ma X. Lead-free halide double perovskites Rb_2InSbX_6 (X = F, Cl, Br, I): A first-principles study of structural and optoelectrical properties. Chem Phys. 2023;573:112015. https://doi.org/10.1016/j.chemphys.2023.112015.

[26] Tang T-Y, Tang Y-L. Physical and optoelectronic properties of double halide perovskites A2CuSbX6 (A = Cs, Rb, K; X = Cl, Br, I) based on first principles calculations. Chem Phys. 2023;570:111897. https://doi.org/10.1016/j.chemphys.2023.111897.

[27] Chen C, Du Y, Xu Y, Wang Z, Tuo Y, Han Z, et al. Machine learning and first-principles study of non-lead-halogen Cs2NaB'Cl6 (B'= In, Cr, Y, Tb) double halide perovskites with optoelectronic properties. Mater Sci Eng B. 2025;316:118138. https://doi.org/10.1016/j.mseb.2025.118138.

[28] Al-Qaisi S, Mushtaq M, Alomairy S, Vu T V, Rached H, Haq BU, et al. First-principles investigations of Na2CuMCl6 (M = Bi, Sb) double perovskite semiconductors: Materials for green technology. Mater Sci Semicond Process. 2022;150:106947. https://doi.org/10.1016/j.mssp.2022.106947.

[29] Zhang Z, Sun Q, Lu Y, Lu F, Mu X, Wei S-H, et al. Hydrogenated Cs2AgBiBr6 for significantly improved efficiency of lead-free inorganic double perovskite solar cell. Nat Commun. 2022;13:3397. https://doi.org/10.1038/s41467-022-31016-w.

[30] Diaz-Morales O, Raaijman S, Kortlever R, Kooyman PJ, Wezendonk T, Gascon J, et al. Iridium-based double perovskites for efficient water oxidation in acid media. Nat Commun. 2016;7:12363. https://doi.org/10.1038/ncomms12363.

[31] Lafler BM, May SJ, Fafarman AT. Role of fluoride and fluorocations in enhanced stability and performance of halide perovskites for photovoltaics. Phys Rev Mater. 2020;4:120301. https://link.aps.org/doi/10.1103/PhysRevMaterials.4.120301.

[32] Hohenberg P, Kohn W. Inhomogeneous Electron Gas. Phys Rev. 1964;136:1–8. https://doi.org/10.1103/PhysRev.136.B864.

[33] Giannozzi P, Baroni S, Bonini N, Calandra M, Car R, Cavazzoni C, et al. QUANTUM ESPRESSO: A modular and open-source software project for quantum simulations of materials. J Phys Condens Matter. 2009;21:395502. https://dx.doi.org/10.1088/0953-8984/21/39/395502.

[34] Jain A, Ong SP, Hautier G, Chen W, Richards WD, Dacek S, et al. The Materials Project: A materials genome approach to accelerating materials innovation. APL Mater. 2013;1:11002. doi: 10.1063/1.4812323.

[35] Prandini G, Marrazzo A, Castelli IE, Mounet N, Marzari N. Precision and efficiency in solid-state pseudopotential calculations. npj Comput Mater. 2018;4. https://doi.org/10.1038/s41524-018-0127-2.

[36] Vanderbilt D. Soft self-consistent pseudopotentials in a generalized eigenvalue formalism. Phys Rev B. 1990;41:7892–5. https://doi.org/10.1103/PhysRevB.41.7892.

[37] Hamann DR, Schlüter M, Chiang C. Norm-Conserving Pseudopotentials. Phys Rev Lett. 1979;43:1494–7. https://doi.org/10.1103/PhysRevLett.43.1494.

[38] Perdew JP, Burke K, Ernzerhof M. Generalized gradient approximation made simple. Phys Rev Lett. 1996;77:3865–8. https://doi.org/10.1103/PhysRevLett.77.3865.

[39] Wu Z, Cohen RE. More accurate generalized gradient approximation for solids. Phys Rev B - Condens Matter Mater Phys. 2006;73:2–7. https://doi.org/10.1103/PhysRevB.73.235116.

[40] Ataua T, Ogunniranye IB, Oyewande OE. Investigation of material properties of halide mixed lead - Free double perovskite for optoelectronic applications using first-principles study. Mater Sci Semicond Process. 2021;133:105963. https://doi.org/10.1016/j.mssp.2021.105963.

[41] Bağcı S, Duman S, Tütüncü HM, Srivastava GP. Electronic and phonon properties of BX (110) (X=P, As, and Sb) and BeY (110) (Y=S, Se, and Te) surfaces. Phys Rev B - Condens Matter Mater Phys. 2009;79:1–13. https://doi.org/10.1103/PhysRevB.79.125326.

[42] Koller D, Tran F, Blaha P. Improving the modified Becke-Johnson exchange potential. Phys Rev B - Condens Matter Mater Phys. 2012;85:1–8. https://doi.org/10.1103/PhysRevB.85.155109.

[43] Madsen GKH, Singh DJ. BoltzTraP. A code for calculating band-structure dependent quantities. Comput Phys Commun. 2006;175:67–71. https://doi.org/10.1016/j.cpc.2006.03.007.

[44] Musembi R, Mbilo M, Nyamuga M, Kachila J. Analysis of Na2CuP ternary semiconductor compound for optoelectronic application by first-principles methods using GGA and mGGA functionals. Comput Condens Matter. 2024;40:e00927. https://doi.org/10.1016/j.cocom.2024.e00927.

[45] Jain A, Ong SP, Hautier G, Chen W, Richards WD, Dacek S, et al. Commentary: The materials project: A materials genome approach to accelerating materials innovation. APL Mater. 2013;1: 011002. https://doi.org/10.1063/1.4812323.

[46] Dai Q, Liang G, Tang T, Gao H, Wu S, Chen Z, et al. Materials Science in Semiconductor Processing Physical properties of novel double perovskite oxides Ba 2 AlXO 6 (X = Nb , Ta) by first-principle calculations. Mater Sci Semicond Process. 2025;185:108930. https://doi.org/10.1016/j.mssp.2024.108930.

[47] Ur Rehman Z, Lin Z. Optoelectronic characteristics and stability evaluation of Ba2TlMxO6 (Mx = Ge, Sn, Se, Te) p-type semiconductors as candidates for functional layers in optoelectronic devices. J Mater Chem C. 2025;5:1–41. https://doi.org/10.1039/D5TC00036J.

[48] Ayyaz A, Murtaza G, Ahmed A, El Ghoul J, Khandaker MU. Revealing vibrational, elastic, electro-optic, and thermoelectric aspects of double perovskites Na2ScCuX6 (X=Cl, Br) for energy harvesting applications by implementing DFT approach. Mater Chem Phys. 2024;325:129808.

https://doi.org/10.1016/j.matchemphys.2024.129808.

[49] Musembi R, Mbilo M. Computational study on structural, elastic, mechanical and optical properties of K_2AgAs ternary semiconductor compound. AIP Adv. 2023;13:115218. https://doi.org/10.1063/5.0170989

[50] Mouhat F, Coudert FX. Necessary and sufficient elastic stability conditions in various crystal systems. Phys Rev B - Condens Matter Mater Phys. 2014;90:1–4. https://doi.org/10.1103/PhysRevB.90.224104.

[51] Hong D, Zeng W, Liu F-S, Tang B, Liu Q-J. The structural, mechanical and electronic properties of NbXSi (X=Fe, Co, Ni, Ru, Rh, Pd, Os, Ir and Pt) compounds from first-principles calculations. Mater Chem Phys. 2021;259:124029. https://doi.org/10.1016/j.matchemphys.2020.124029.

[52] Kholil MI, Bhuiyan MTH. Electronic, elastic, vibrational and superconducting properties of a ternary superconductors LaIrP (P = P, As): Insights from DFT. Solid State Commun. 2020;322:114053. https://doi.org/10.1016/j.ssc.2020.114053.

[53] Kumar V, Singh BP. Structural and elastic properties of AIBIIIC 2VI semiconductors. Indian J Phys. 2018;92:29–35. https://doi.org/10.1007/s12648-017-1082-3.

[54] Caid M, Rached D, Rached Y, Rached H. Comprehensive exploration of halide double perovskites Cs_2BGeCl_6 (B: Zn, Cd) for affordable energy technologies: a high-throughput investigation. Opt Quantum Electron. 2024;56:1–22. https://doi.org/10.1007/s11082-024-06721-z.

[55] Datta AK, Hossain MK, Rahman MS, Paramasivam P, El-marghany A, Mishra VK. DFT insights into bandgap engineering of lead-free $LiMCl_3$ (M = Mg, Be) halide perovskites for optoelectronic device applications. Sci Rep. 2025;15:1–19. https://doi.org/10.1038/s41598-025-80621-z.

[56] Gaillac R, Pullumbi P, Coudert FX. ELATE: An open-source online application for analysis and visualization of elastic tensors. J Phys Condens Matter. 2016;28: 275201. https://dx.doi.org/10.1088/0953-8984/28/27/275201.

[57] Abbas Z, Islam N, Aslam M, Parveen A, Al-Qaisi S, Muhammad S, et al. DFT insights for structural, opto-electronic, thermodynamic and transport characteristics of Tl_2TeX_6 (X = At, Br, Cl, I) double perovskites for low-cost solar cell applications. Inorg Chem Commun. 2024;163:112293. https://doi.org/10.1016/j.inoche.2024.112293.

[58] Liang QQ, Hu DY, Tang TY, Gao HX, Wu SQ, Li L, et al. First-principles calculations to investigate structural, electronic, optical and thermodynamic properties of anti-perovskite compounds X_3OI(X = Na, K, Rb). J Mater Res Technol. 2023;22:3246–3254. https://doi.org/10.1016/j.jmrt.2022.12.148.

[59] Kumar A, Ahmad Sofi S, Chandel T, Thakur N. First-principles calculations to investigate structural stability, half-metallic behavior, thermophysical and thermoelectric properties of Co_2YAl (Y = Mo, Tc) full Heusler compounds.

Comput Theor Chem. 2023;1219:113943. https://doi.org/10.1016/j.comptc.2022.113943.

[60] Srivastava A, Sarkar P, Tripathy SK, Lenka TR, Menon PS. Structural, electronic and optical properties of Ag2MgSn(S/Se)4 quaternary chalcogenides as solar cell absorber layer: An Ab-initio study. Sol Energy 2020;209:206–213. https://doi.org/10.1016/j.solener.2020.08.094.

[61] Bhattacharjee R, Chattopadhyaya S. Effects of barium (Ba) doping on structural, electronic and optical properties of binary strontium chalcogenide semiconductor compounds - A theoretical investigation using DFT based FP-LAPW approach. Mater Chem Phys. 2017;199:295–312. http://dx.doi.org/10.1016/j.matchemphys.2017.06.057.

[62] Ciftci YO, Colakoglu K, Korozlu NS. First principles studies of elastic, electronic and optical properties of chalcopyrite semiconductor ZnSnP 2. J Alloys Compd . 2012;529:1–7. http://dx.doi.org/10.1016/j.jallcom.2012.03.045.

[63] Nazir G, Tariq S, Afaq A, Mahmood Q. Under pressure DFT investigations on optical and electronic properties of PbZrO3. Acta Phys Pol A. 2018;133:105–113. doi: 10.12693/APhysPolA.133.105.

[64] Oddi F, Lakel S, Benramache S, Almi K. First Principles Study on Electronic Structure and Optical Properties of Ternary Semiconductor InxAl1 –xP Alloys. Semiconductors. 2020;54:59–66. https://doi.org/10.1134/S1063782620010182.

[65] Yaseen MS, Sun J, Fang H, Murtaza G, Sholl DS. First-principles study of electronic and optical properties of ternary compounds AuBX2 (X = S, Se, Te) and AuMTe2 (M = Al, In, Ga). Solid State Sci . 2021;111:106508. https://doi.org/10.1016/j.solidstatesciences.2020.106508.

[66] Houmad M, Dakir O, Abbassi A, Benyoussef A, El Kenz A, Ez-Zahraouy H. Optical properties of SiC nanosheet. Optik (Stuttg). 2016;127:1867–1870. http://dx.doi.org/10.1016/j.ijleo.2015.11.017.

[67] Ejjabli A, Karouchi M, Al-Hattab M, Bajjou O, Rahmani K, Lachtioui Y. Investigation of lead-free halide K2AgSbBr6 double Perovskite's structural, electronic, and optical properties using DFT functionals. Chem Phys Impact. 2024;9:100658. https://doi.org/10.1016/j.chphi.2024.100658.

[68] Mia MH, Khatun MA. Dynamic tuning of optoelectronic and mechanical properties in TlMCl3 (M = Ge, Sn) under pressure-induced phase transition. Heliyon. 2025;11:e42603. https://doi.org/10.1016/j.heliyon.2025.e42603.

[69] Ajay G, Sirajuddeen MMS, Ashwin V. First-principles investigation of structural, electronic, and optical properties of cubic halide perovskite RbSrI3. Chem Phys Impact. 2024;8:100431. https://doi.org/10.1016/j.chphi.2023.100431.

[70] Jehan A, Husain M, Tirth V, Algahtani A, Uzair M, Rahman N, et al. Investigation of the structural, electronic, mechanical, and optical properties of NaXCl3 (X = Be, Mg) using density functional theory. RSC Adv.

2023;13:28395–28406. https://doi.org/10.1039/D3RA04922A.

[71] Dixit A, Annie Abraham J, Manzoor M, Altaf M, Anil Kumar Y, Sharma R. A comprehensive DFT analysis of the physical, optoelectronic and thermoelectric attributes of Ba_2InNbO_6 double perovskites for eco-friendly technologies. Mater Sci Eng B. 2024;307:117530. https://doi.org/10.1016/j.mseb.2024.117530.

[72] Dahbi S, Tahiri N, El Bounagui O, Ez-Zahraouy H. Effects of oxygen group elements on thermodynamic stability, electronic structures and optical properties of the pure and pressed $BaTiO_3$ perovskite. Comput Condens Matter. 2022;32:e00728. https://doi.org/10.1016/j.cocom.2022.e00728.

[73] Azahaf C, Zaari H, Abbassi A, Ez-Zahraouy H, Benyoussef A. Theoretical investigation of spontaneous polarization, electronic and optical properties of cubic perovskite $BaHfO_3$. Opt Quantum Electron. 2015;47:2889–2897. https://doi.org/10.1007/s11082-015-0176-2.

[74] Dai Q, Liang Q-Q, Tang T-Y, Gao H-X, Wu S-Q, Tang Y-L. Insights on structural, elastic, electronic, optical and thermodynamic properties and population analysis of double perovskite oxide Ba_2MgXO_6 (X = Se, Te). Mater Sci Semicond Process. 2024;171:108003. https://doi.org/10.1016/j.mssp.2023.108003.

[75] Shirodkar S, Prabhu AN, Putran S, Rao A, Shanubhogue UD, Hegde GS. Potential improvement in power factor of $(Bi_{0.98}Ga_{0.02})_2Te_{2.7}Se_{0.3}$ compound due to defect engineering. J Mater Sci Mater Electron. 2024;35:1–12. https://doi.org/10.1007/s10854-024-12673-7.

[76] Gurung T, Jagan R, Shanubhogue U D, Poojitha G, Poorneeh P, Rao A. Enhancement in power factor through rare-earth samarium doping in Cu_2SnSe_3 system. Phys Scr. 2024;99:105908. https://dx.doi.org/10.1088/1402-4896/ad7208.

[77] Basit Shakir M, Murtaza G, Ayyaz A, Khan H, Touqir M, Naeem M, et al. Probing the Structural, Electronic, Thermodynamic, Optical, and thermoelectric features of Lead-Free double perovskites Na_2ScAgZ_6 (Z=Br, I) for green energy harvesting. Inorg Chem Commun. 2024;168:112932. https://doi.org/10.1016/j.inoche.2024.112932.

[78] Berri S, Bouarissa N. Density functional theory calculations of electronic structure and thermoelectric properties of K-based double perovskite materials. Energy Storage. 2023;5:e400. https://doi.org/10.1002/est2.400.

[79] Manzoor M, Hussain M, Aslam M, Evgeny B, Sharma R, Alshomrany AS, et al. Tailoring the physical, optoelectronic and transport properties of novel lead-free Sodium perovskites Na_2TeX_6 (X = Cl, Br, I) using DFT computation for photovoltaic and thermal devices. Chinese J Phys. 2024;89:1333–1346. https://doi.org/10.1016/j.cjph.2024.02.027.

[80] Yadav A, Deshmukh PC, Roberts K, Jisrawi NM, Valluri SR. An analytic study

of the Wiedemann–Franz law and the thermoelectric figure of merit. J Phys Commun. 2019;3: 105001. https://dx.doi.org/10.1088/2399-6528/ab444a.

[81] Togo A, Chaput L, Tadano T, Tanaka I. Implementation strategies in phonopy and phono3py. J Phys Condens Matter. 2023;35:353001. https://dx.doi.org/10.1088/1361-648X/acd831.

[82] Shen K, Ren Q, Zhao L, Qiu Y, Yao X, Jiang P, et al. Point Defects Enhance Cross-Plane Thermal Conductivity in Graphite. Adv Mater. 2025;37:2410669. https://doi.org/10.1002/adma.202410669.

[83] Irfan S, Yan Z, Khan SB. Advancements in thermoelectric materials: A comprehensive review. Mater Sci Energy Technol. 2024;7:349–373. https://doi.org/10.1016/j.mset.2024.06.002.

[84] Singh R, Dogra S, Dixit S, Vatin NI, Bhardwaj R, Sundramoorthy AK, et al. Advancements in thermoelectric materials for efficient waste heat recovery and renewable energy generation. Hybrid Adv. 2024;6:100176. https://doi.org/10.1016/j.hybadv.2024.100176.

[85] Ullah R, Ali MA, Haq BU, Khan A, Mahmood Q, Murtaza G. Exploring electronic, structural, magnetic and thermoelectric properties of novel Ba2EuMoO6 double perovskite. Mater Sci Semicond Process. 2022;137:106218. https://doi.org/10.1016/j.mssp.2021.106218.

- GGA predicts structural, thermodynamic, and mechanical stability of Rb_2NaInF_6.
- Band gap ranges from 2.14 to 3.76 eV using various DFT approximations.
- Strong optical absorption in the 6–20 eV range indicates UV absorber potential.
- Lead-free Rb_2NaInF_6 shows a high ZT value of 0.83 above 900 K.

Insights into the Optoelectronic and Thermoelectric Properties of Lead-Free Rb_2NaInF_6 Double Perovskite: A First-Principles Study

Mesande Mbilo[a,*], Robinson Musembi[b], John Kachilu[a,*], Wesley Omasta[c], Fanuel Mugwanga[a], Refilwe Edwin Mapasha[d]

[a]Department of Physics and Sustainable Technology, School of Pure and Applied Sciences, Pwani University, P.O. Box 195-80108, Kilifi, Kenya

[b]Materials Research Group, Department of Physics, Faculty of Science and Technology, University of Nairobi, P.O. Box 30197 – 00100, Nairobi, Kenya

[c]Department of Physics, Mbeya University of Science and Technology, P.O. Box 131, Mbeya, Tanzania

[d]Department of Physics, University of Pretoria, Hatfield campus, Pretoria 0002, South Africa

*Corresponding Author: [illegible]@gmail.com

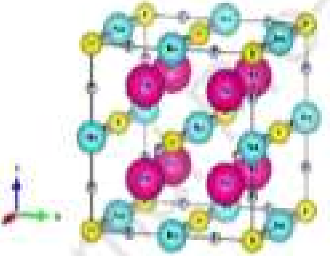

Fig. 1. Crystal structure of the Rb$_2$NaInF$_6$ lead-free double perovskite compound

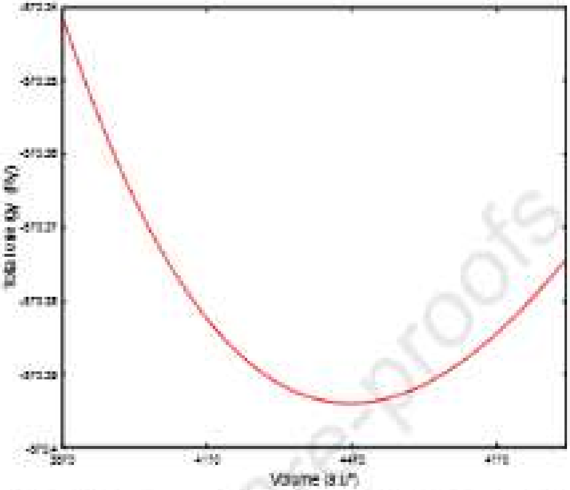

Fig. 2. Birch-Murnaghan equation of state fit plots of the Rb_2KAlF_6 lead-free double perovskite compound.

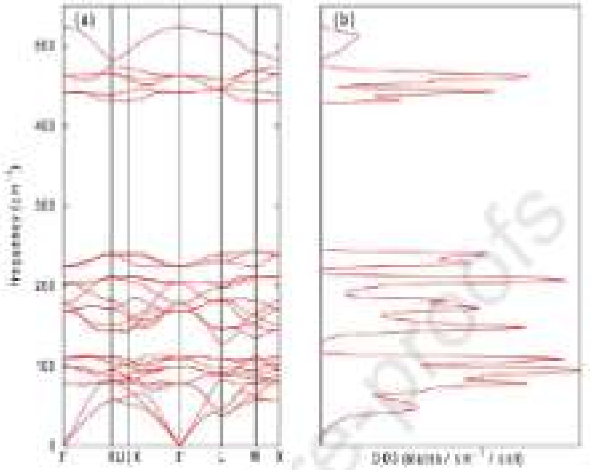

Fig. 3. GGA-PBE (a) phonon dispersion and (b) density of states curves of Rb$_2$NaIrF$_6$ lead-free double perovskite compound.

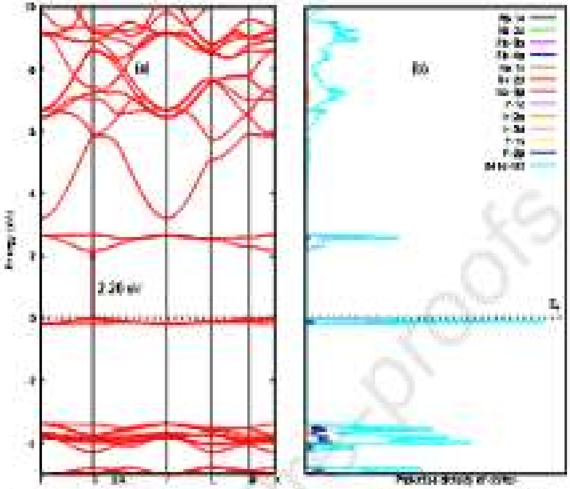

Fig. 4. The GGA-PBE (a) electronic band structure and (b) projected density of states of Rb_2NaInF_6 lead-free double perovskite compound.

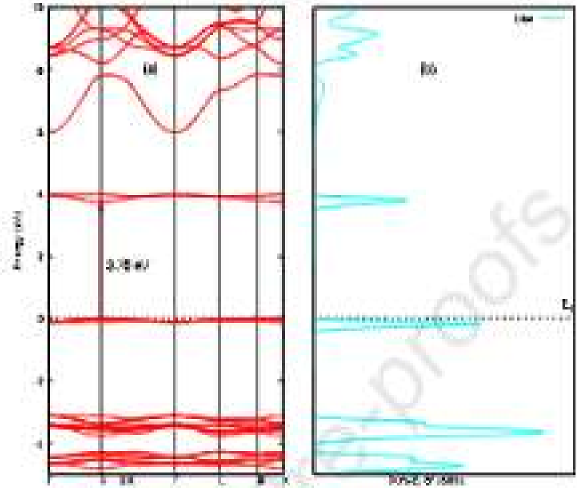

Fig. 5. The TB-mBJ (a) electronic band structure and (b) density of states of the Rb_2NaInF_6 lead-free double perovskite compound.

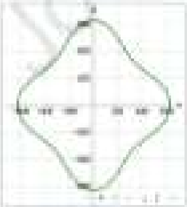

(a) Young's modulus in xy

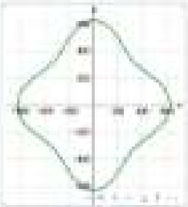

Young's modulus in xz

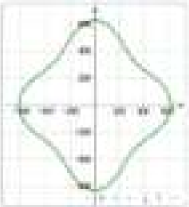

Young's modulus in yz

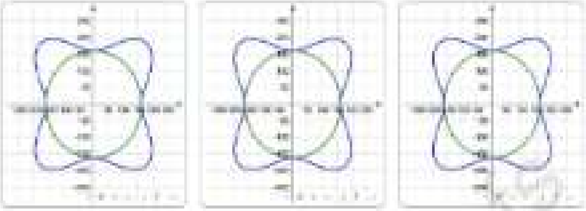

(b) Shear modulus in xy Shear modulus in xz Shear modulus in yz

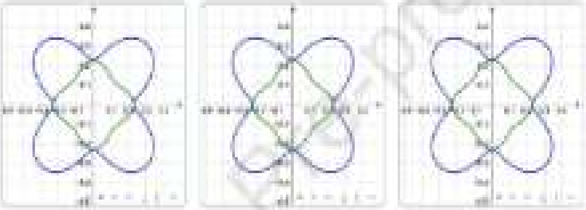

(c) Poissons Ratio in xy Poissons Ratio in xz Poissons Ratio in yz

Fig. 6. Two-dimensional spatial dependence maps of (a) Young's modulus, (b) shear modulus, and (c) Poisson's ratio of the Rb$_2$NaInF$_6$ lead-free double perovskite compound.

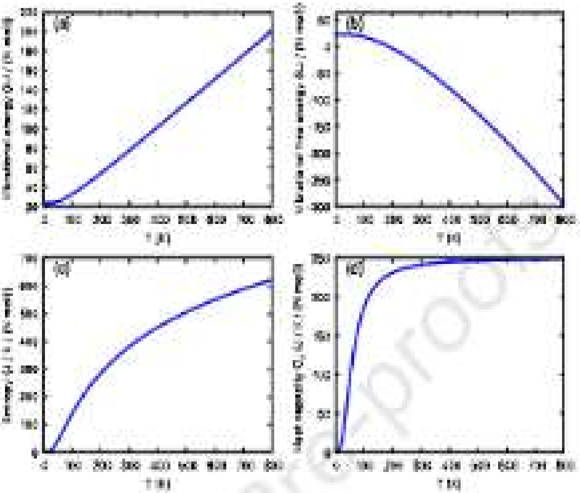

Fig. 7. Thermodynamic properties of Rb_2KAlF_6 lead-free double perovskite compound: (a) vibrational energy, (b) vibrational free energy, (c) entropy, and (d) heat capacity as a function of temperature.

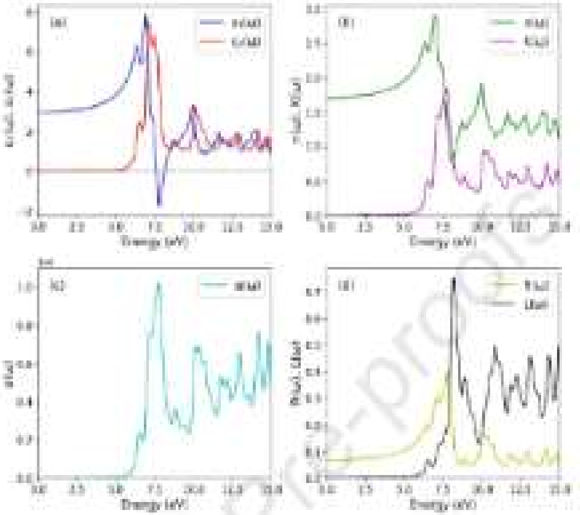

Fig. 8. The optical properties of the Rb_2NaInF_6 lead-free double perovskite compound computed using the GGA-PBE approximation. (a) $\varepsilon_1(\omega)$ and $\varepsilon_2(\omega)$, (b) $n(\omega)$ and $K(\omega)$, (c) $\alpha(\omega)$, and (d) $R(\omega)$ and $L(\omega)$.

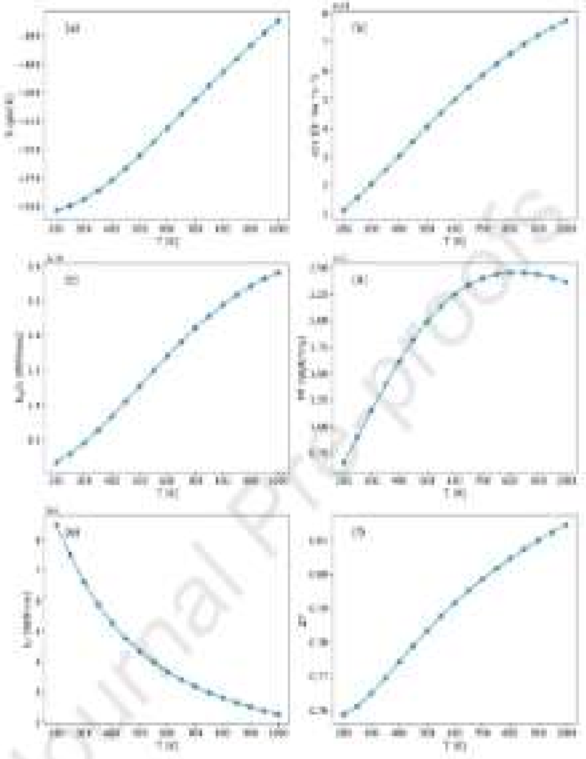

Fig. 9. The thermoelectric properties of the Rb_2NaInF_6 lead-free double perovskite compound. (a) Seebeck coefficient (S), (b) Electrical conductivity (σ/τ), (c) Electronic thermal conductivity (κ_e/τ), (d) Power factor (PF), (e) Lattice thermal conductivity (κ_L), and (f) Figure of merit (ZT).

Insights into the Optoelectronic and Thermoelectric Properties of Lead-Free Rb_2NaIrF_6 Double Perovskite: A First-Principles Study

Mwende Mbilo[a,*], Robinson Musembi[b], John Kachira[c,*], Wesley Onsate[b], Fanuel Mugwanga[b], Refilwe Edwin Mapasha[d]

[a]Department of Physics and Sustainable Technology, School of Pure and Applied Sciences, Pwani University, P.O. Box 195-80108, Kilifi, Kenya

[b]Materials Research Group, Department of Physics, Faculty of Science and Technology, University of Nairobi, P.O. Box 30197 – 00100, Nairobi, Kenya

[c]Department of Physics, Mbeya University of Science and Technology, P.O. Box 131, Mbeya, Tanzania

[d]Department of Physics, University of Pretoria, Hatfield campus, Pretoria 0002, South Africa

*Corresponding Author: mwendembilo@gmail.com

Table 1. Structural properties of Rb_2NaIrF_6 lead-free double perovskite compound.

	GGA-PBE	Other works [45]
Equilibrium Energy E_0 (Ry)	-570.39	
Lattice parameter a_0 (a.u)	16.45	16.44
Equilibrium volume V_0 (a.u^3)	4451.54	4435.15
t_F	0.99	
μ	0.54	
Energy of formation ΔH_f (Ry)	-1.87	

Table 2. The electronic band gaps of the Rb_2NaIrF_6 lead-free double perovskite compound calculated using different approximations.

Methods	Band gaps (eV)
GGA-PBE	2.20
GGA-WC	2.14
R2SCAN	2.78
TB-mBJ	3.76
ML	2.33
Other works [34]	2.40

Table 3. Elastic tensor (C_{ij}) in GPa for the Rb_2NaIrF_6 cubic crystal structure.

	C_{11}	C_{12}	C_{44}
GGA-PBE	71.36	21.97	15.95

Table 4. Computed mechanical properties: bulk modulus B, Young's modulus E, Shear modulus G, Pugh's ratio B/G, Poisson's ratio n, Anisotropy factor A, Debye velocity V_m, and Debye temperature θ_D of Rb_2NaIrF_6 lead-free double perovskite compound.

	B	E	G	B/G	n	A	V_m(m/s)	θ_D(K)

GGA-PBE	38.43	45.87	19.02	2.02	0.28	0.66	2156.45	252.47